Communication

Design of a Vivaldi-Fed Hybrid Horn Antenna for Low-Frequency Gain Enhancement

Tae Heung Lim, Jong-Eon Park, and Hosung Choo

***Abstract*— This communication proposes the hybrid Vivaldi-fed horn antenna, which consists of the printed antipodal Vivaldi antenna (AVA) on an FR4 substrate for better matching performance in the low-frequency band and the horn antenna that surrounds the exterior of the AVA for increased gain performance in the high frequency. In order to verify the operating principle in the low-frequency band, an equivalent circuit of the proposed antenna is modeled and analyzed. The mode decomposition technique is then used to examine the radiation physics of the proposed antenna in high-frequency band. The measured reflection coefficients in the entire frequency range are less than −3 dB of the half-power reference (maximum of −4.11 dB). The measured gains of 2.12 dBi at 1 GHz and 7.84 dBi at 6 GHz are obtained. These results confirm that the better characteristics in low-frequency matching and high-frequency gain can be achieved by the proposed design.**

***Index Terms*— Antipodal Vivaldi antenna (AVA), horn antennas, hybrid antenna, Vivaldi antennas.**

I. Introduction

Vivaldi antennas with a co-planar structure have been widely used in various applications for their simple planar structure and broadband characteristic [1]. The basic structure evolved later into an antipodal Vivaldi antenna (AVA) [2], which has advantages in ultrawide bandwidth and ease of matching with a coaxial feed system. The AVA has been widely adopted for many applications, such as medical microwave imaging [3], radar systems [4], automotive applications [5], and satellite communications systems [6]. However, due to pattern distortions such as a beam split and a low front-to-back ratio, the AVA often shows gain degradation as the frequency increases. To resolve the gain deterioration in the high-frequency band, various studies on the AVA have been conducted, such as printed flares with slots [7], attaching a lens [8], inserting a parasitic ellipse [9], and optimizing the shape of flares [10], [11]. On the other hand, horn antennas that are typically used in measurement setup in microwave frequency bands [12] have a high-gain property with a relatively wide bandwidth [13], [14]. However, a typical horn antenna needs an extremely large aperture in order to operate with a proper gain in the low frequency range. To decrease the size of the horn aperture, many studies have been recently carried out such as the loading with absorbing materials and metamaterials [15], [16], the miniaturized water-filled ridged horn antenna [17], and compact design TEM horn antenna [18]. Based on the aforementioned AVA and horn characteristics, we can expect that the best results can be achieved by hybridizing the advantages of both antennas, but in-depth hybrid studies of AVA and horn have not been conducted yet.

In this communication, to resolve these problems, we propose a hybrid Vivaldi-fed horn antenna, which has the advantage of the AVA in the low-frequency band and the advantage of the horn in the high-frequency band. The AVA in the antenna consists of a parallel transmission line and radiating flares, which are printed on FR4 substrates. The exterior of the AVA is surrounded by a horn antenna for better gain performance in the high frequency, and the two ends of the flares of the AVA are then electrically connected to the external horn for better impedance matching in the low-frequency band. The proposed antenna shows a better boresight gain property compared to the conventional AVA or a horn antenna [19]. The detailed design parameters of the antenna are optimized using the FEKO EM simulation software [20]. In order to verify the operating principle of the AVA in low-frequency band, an equivalent circuit of the proposed antenna is modeled and compared with a conventional AVA [21]. The mode decomposition technique is then used at the antenna aperture to examine the radiation physics of the proposed antenna in high frequency range, which represents a TE_{10} mode similar to the traditional horn antenna. These results confirmed that the low frequency matching and high-frequency gain characteristics can be improved by the proposed design.

II. Antenna Structure and Measurement

A. Structure of the Proposed Antenna

Fig. 1 shows the conceptual geometry of the proposed hybrid Vivaldi-fed horn antenna. In the proposed antenna structure, the AVA is employed and used as the feed for achieving better impedance matching in the low-frequency band, while the horn is adopted in the exterior of the AVA to obtain higher directive gain in the high-frequency band. Thus, the antenna can be considered as two major parts consisting of the Vivaldi and the horn. The Vivaldi part is then divided into three subsections of a balun, a parallel plate transmission line, and flares. All three sections are printed on an FR4 thin substrate ($\varepsilon_r = 4.4$ and $\tan\ \delta = 0.0018$) with a thickness of h. The balun in the first section has a length of l_1 and operates as a transition between a single-ended coaxial feed and the balanced transmission line in the second section. The ground width of the balun is linearly tapered from b_1 to t for the length of l_2. The width t of the microstrip line is determined using the basic microstrip line equations [22]. Then, the balanced parallel plate transmission line with the length of l_3 delivers the input power from the balun to the flares with the impedance matching

$$Z(z) = Z_0 e^{a(z-l_1)} \quad \text{for} \quad l_1 < z < l_1 + l_3 \tag{1a}$$

Manuscript received February 16, 2017; revised September 25, 2017; accepted October 28, 2017. Date of publication November 22, 2017; date of current version January 2, 2018. This work was supported in part by the National Research Foundation of Korea (NRF) grant funded by the Ministry of Science and Information and Communication Technology under Grant NRF-2017R1A5A1015596 and in part by the Basic Science Research Program through the NRF funded by the Ministry of Education under Grant 2015R1A6A1A03031833. *(Corresponding author: Jong-Eon Park.)*

T. H. Lim and H. Choo are with the School of Electronic and Electrical Engineering, Hongik University, Seoul 04066, South Korea.

J.-E. Park is with the Metamaterial Electronic Device Research Center, Hongik University, Seoul 04066, South Korea (e-mail: jongeon.park@gmail.com).

Color versions of one or more of the figures in this communication are available online at http://ieeexplore.ieee.org.

Digital Object Identifier 10.1109/TAP.2017.2776608

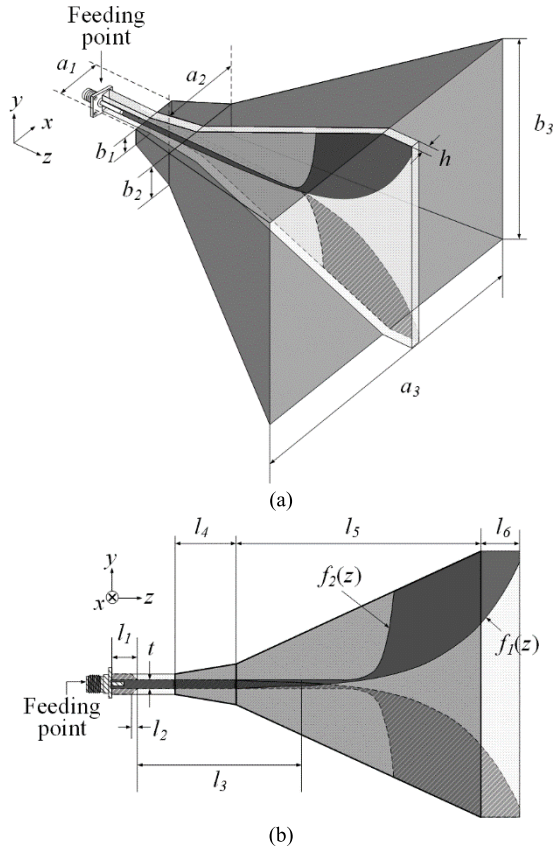

Fig. 1. Configuration of the proposed Vivaldi-fed hybrid horn antenna. (a) Perspective view. (b) Side view.

where $a = (1/l_3)\ln\left((Z_L/Z_0)\right)$

$$\Gamma(\psi) = \Gamma(2\beta z) = \frac{1}{2}\sum_{n=0}^{N} e^{-2j\beta n\Delta z}\left[\frac{d}{dz}\ln\left(\frac{Z(z)}{Z_0}\right)\right]_{z=n\Delta z}\Delta z \tag{1b}$$

where $\psi = 2\beta z, z = n\Delta z, n = 0, 1, \ldots, N$.

The reflection coefficient in (1b) at the start point of the transmission line is then obtained by summation of the impedance of (1a). Δz is the discrete piece of the tapered transmission line. Z_0 is a characteristic impedance of 50 Ω and Z_L is the input impedance seen from the location at $z = l_1 + l_3$. Finally, the width of the transmission line at the location z can now be obtained by the tapered transmission line theory [22]. In the third section, the conducting flares are designed by exponential functions $f_1(z)$ and $f_2(z)$ to improve the low frequency characteristics by operating as a resonant antenna, where the low-end frequency is determined approximately by the width of b_3 as a half-wavelength [9]. The exponential form of the flares is essentially useful for broadband matching with the intrinsic impedance of free space, where the functions for flare geometry are written as follows:

$$f_1(z) = c_1 e^{c_2(z-(l_1+l_3))} - c_3 \tag{2a}$$
$$f_2(z) = c_4 e^{c_5(z-(l_1+l_3))} + c_6. \tag{2b}$$

The second part, the horn is divided into two subsections with different slopes in pyramidal shapes. The first section with a low slope in the shape is necessary for improving the impedance matching up to the required high-end frequency. The aperture area of $a_1 \times b_1$ linearly increases to $a_2 \times b_2$ for the horn length of l_4. Then, the second section is added to provide the required aperture area to obtain the needed gain at the low-end frequency, and the area increases to $a_3 \times b_3$ for the horn length of l_5. The design parameters of the horn are determined by the basic calculation formula of the pyramidal horn antennas [23]

$$\left(\sqrt{2\chi} - \frac{b_1}{\lambda}\right)^2 (2\chi - 1) = \left(\frac{G_0}{2\pi}\sqrt{\frac{3}{2\pi}}\frac{1}{\sqrt{\chi}} - \frac{a_1}{\lambda}\right)^2 \left(\frac{G_0^2}{6\pi^3}\frac{1}{\chi} - 1\right) \tag{3a}$$

$$\frac{\rho_e}{\lambda} = \chi, \quad \frac{\rho_h}{\lambda} = \frac{G_0^2}{8\pi^3}\left(\frac{1}{\chi}\right) \tag{3b}$$

$$\rho_h \approx \sqrt{(l_4 + l_5)^2 + \left(\frac{a_3}{2}\right)^2}$$
$$\rho_e \approx \sqrt{(l_4 + l_5)^2 + \left(\frac{b_3}{2}\right)^2} \tag{3c}$$

$$a_3 \approx \sqrt{3\lambda\rho_h} = \frac{G_0}{2\pi}\sqrt{\frac{3}{2\pi\chi}}\lambda$$
$$b_3 \approx \sqrt{2\lambda\rho_e} = \sqrt{2\chi\lambda} \tag{3d}$$

where G_0 is the desired gain of the horn at the wavelength λ at the high-end frequency. ρ_e is the overall slope length of the horn in the x-axis and ρ_h is the total slope length of the horn in the y-axis. The external conducting horn allows the electromagnetic fields to be guided as the dominant TE mode up to the required high-end frequency. Finally, the external horn and the AVA are hybridized by electrically connecting the top and bottom of the horn to the two flares of the AVA. In particular, the horn is divided by the substrate of thickness h into two parts, as shown in Fig. 1(a), one in the left and the other in the right. The upper and lower flares of the AVA are electrically connected separately to the left and right parts of the horn, respectively. These connections enlarge the electrical length of the AVA flares, resulting in the improved impedance matching in the low-frequency band. In addition, the flares are protruded by the length of l_6 from the horn aperture to increase the electrical length for better low frequency characteristics.

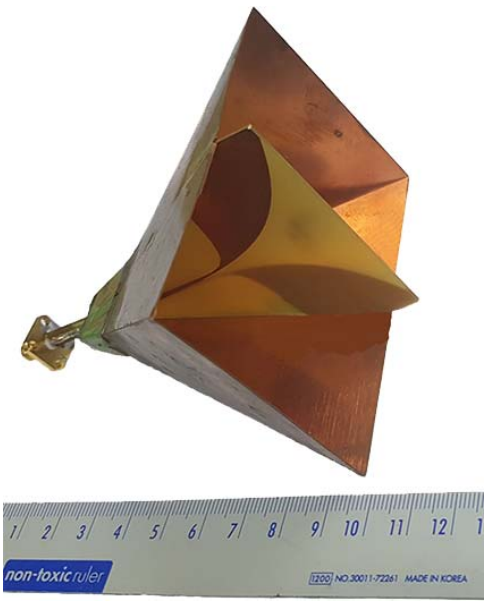

Fig. 2. Photograph of the fabricated antenna.

Fig. 2 illustrates a photograph of the fabricated antenna, and the detailed design parameters are listed in Table I. A SJ-408-093 50 Ω SMA connector is used for the coaxial feeder of the antenna. The balun, transmission line, and flares of the AVA are fabricated by

TABLE I
DESIGN PARAMETERS OF THE PROPOSED ANTENNA

Parameters or functions	Optimized values or curves
a_1	1 mm
b_1	5 mm
a_2	29 mm
b_2	13 mm
a_3	98 mm
b_3	65 mm
h	1 mm
l_1	10 mm
l_2	0.5 mm
l_3	42.5 mm
l_4	15 mm
l_5	60 mm
l_6	9.5 mm
t	2 mm
c_1	0.115
c_2	0.035
c_3	1.115
c_4	3.23×10^{-9}
c_5	0.23
c_6	1

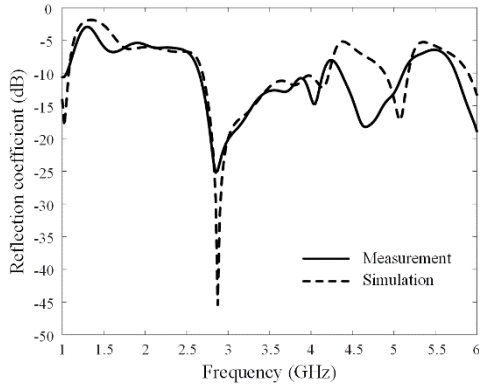

Fig. 3. Simulated and measured reflection coefficients of the proposed antenna.

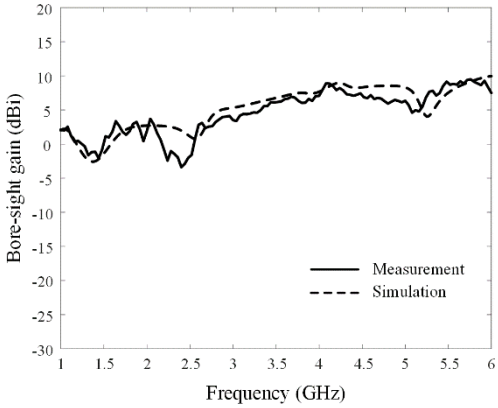

Fig. 4. Simulated and measured boresight gains of the proposed antenna.

etching the metallic surface on the 1 mm FR4-substrate, and the horn is made by bending the copper plates with a thickness of 0.4 mm. The AVA and the horn are electrically connected by soldering flares and the copper plates.

B. Measurement of the Proposed Antenna

Fig. 3 illustrates the reflection coefficients of the proposed antenna and shows the measured values of −10.6 and −17.9 dB at 1 and 6 GHz, respectively. The reflection coefficients in the entire frequency range are less than −3 dB of the half-power reference (maximum of −4.11 dB). Fig. 4 represents the measured boresight gain in comparison with the simulation. The measured results show good agreement with simulation, and the values of the boresight gains

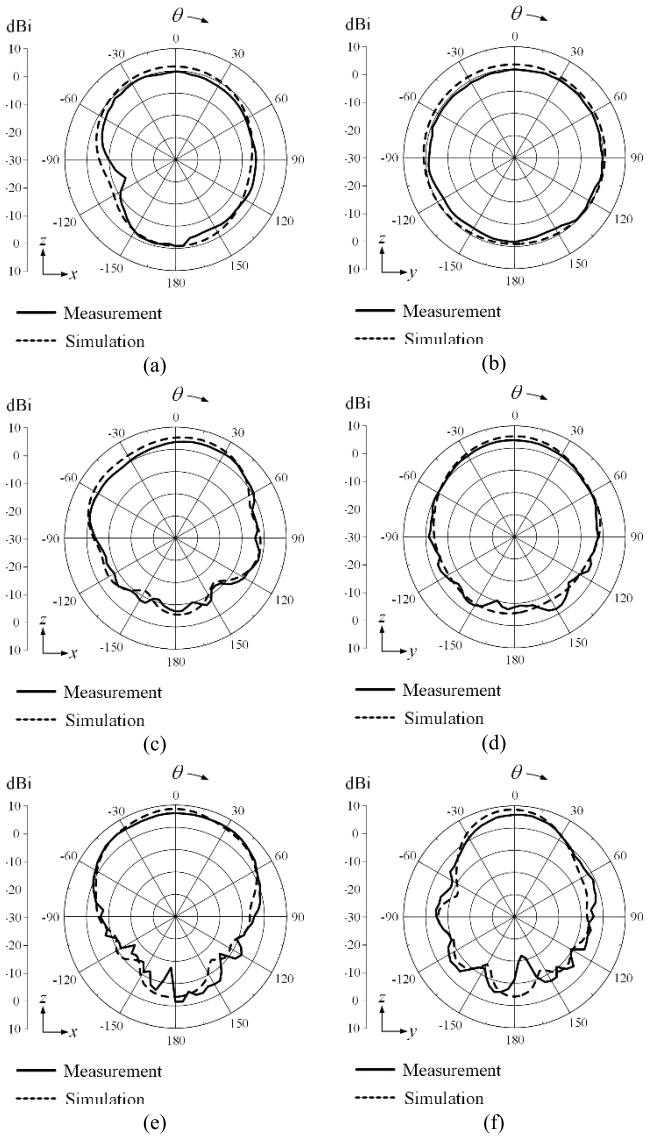

Fig. 5. Measurement and simulation of the radiation patterns in *zx* and *zy* planes. (a) and (b) 1 GHz. (c) and (d) 3 GHz. (e) and (f) 5 GHz.

TABLE II
ANTENNA PERFORMANCES

Operating frequency range	1 GHz – 6 GHz (VSWR < 4.5)
Antenna size	98 mm × 65 mm × 100 mm
VSWR (max, min)	4.3, 1.1
Gain (max, min)	9.4 dBi, –3 dBi
HPBW (max, min)	130°, 38.4°
SLL (max, min)	12 dB, 3.2 dB
Polarization	Linear

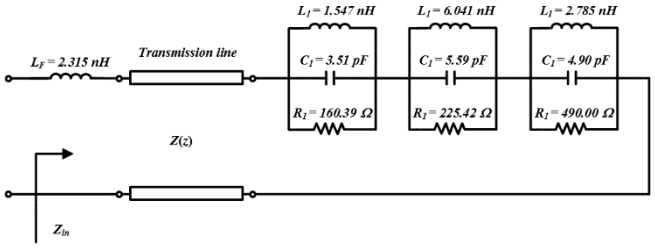

Fig. 6. Equivalent circuit model of the proposed antenna.

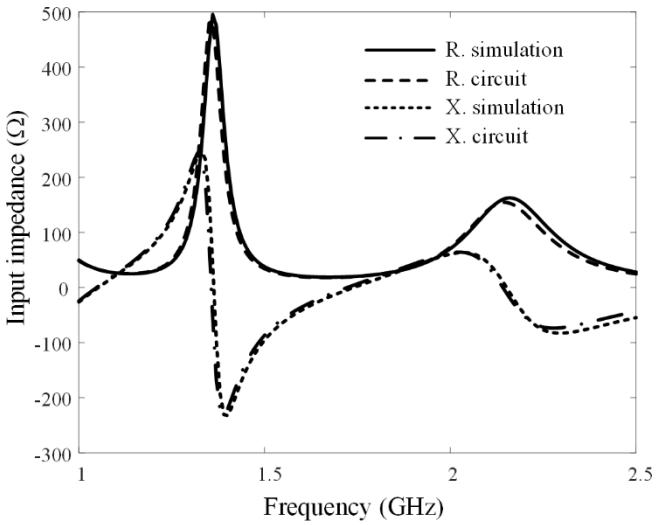

Fig. 7. Input impedance of the proposed antenna from the EM simulation and the equivalent circuit model (R: Resistance and X: Reactance).

are 2.12 dBi at 1 GHz and 7.84 dBi at 6 GHz. The resulting gain at low-end frequency is higher than the conventional horn antenna [23], and the gain at high-end frequency is better than the conventional AVA [24]. The measured boresight gain shows good agreement with the simulation in the low frequency range below 3.5 GHz. Some discrepancies are observed above 3.5 GHz and are due to the slight difference between the simulation and fabrication of the antenna, which are sensitive in the high frequency range. As expected, the improvement in the low frequency comes from the impedance matching by enlarging the electrical length of the AVA while the high-frequency gain enhancement is achieved by adopting the high-directivity characteristics of the traditional horn antenna. Fig. 5(a)–(f) presents the simulated and measured radiation patterns in the *zx* and *zy* planes at 1, 3, and 5 GHz, respectively. Since the horn part enhances the directivity in the high frequency range, the half-power beamwidth becomes narrower as the frequency increases in the *zy* plane. Brief antenna performances are listed in Table II.

III. Analyses Using Equivalent Circuit and Mode Decomposition

A. Analysis Using Equivalent Circuit

To examine the operating principle of the antenna at the low frequencies, an equivalent circuit model with lumped elements is suggested as shown in Fig. 6. The inductance L_F is inserted to represent the balun with length l_1 and the SMA connector. The balanced parallel transmission line of length l_3 in the AVA is employed, where the impedance is a function of the location z, as introduced in (1a). The three parallel combinations of *RLC* elements are then used to operate as a resonant antenna in the low-frequency band. The input impedances Z_{in} (both resistance and reactance) of the equivalent circuit are plotted in Fig. 7. As can be seen, both curves from the equivalent circuit and the electromagnetic simulation are in good agreement with each other and show about 50 Ω input resistance at 1 and 2 GHz. The first elements (L_1, C_1, and R_1) represent the resonance below 1 GHz, and the second (L_2, C_2, and R_2) and the third (L_3, C_3, and R_3) elements indicate the resonances at 1.36 and 2.16 GHz, respectively. The characteristics of the input impedance demonstrate that the operating principle of the proposed antenna in the low-frequency band is similar to that of a conventional Vivaldi antenna.

B. Mode Decomposition

To analyze the radiating principle of the proposed antenna in the high-frequency band, the mode decomposition of the E_y-field at the aperture $a_3 \times b_3$ is conducted by a data fitting method. The two flares printed on the AVA, which are located vertically in the center of the aperture, enhance the TE_{10} mode and this operation is similar with the ridges in the double-ridged horn antenna [25]. The dominant mode is concentrated in the center of the aperture and increases the boresight gain, especially in the high-frequency band. Fig. 8(a) and (b) shows the y-component of the electric field observed at $z = 90.5$ mm (0 mm $\leq x \leq$ 98 mm and 0 mm $\leq y \leq$ 65 mm) with 99 $\times$ 66 points at 2 and 4 GHz, respectively. To accurately analyze the modes of the proposed antenna, the E_y-field magnitudes are examined in the line segments $\overline{AA'}$, $\overline{BB'}$, $\overline{CC'}$, and $\overline{DD'}$. The mode decomposition of the E_y-field magnitudes is carried out using the nonlinear least squares of the sum of harmonic

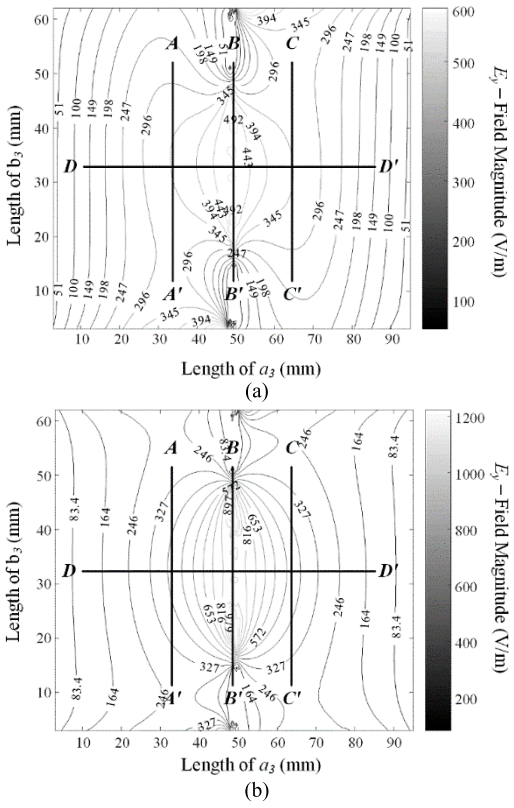

Fig. 8. E_y-field distributions at the open cross section $a_3 \times b_3$ of the proposed antenna. The magnitude of E_y-field on the $\overline{AA'}$, $\overline{BB'}$, $\overline{CC'}$, and $\overline{DD'}$ are measured. (a) 2 GHz. (b) 4 GHz.

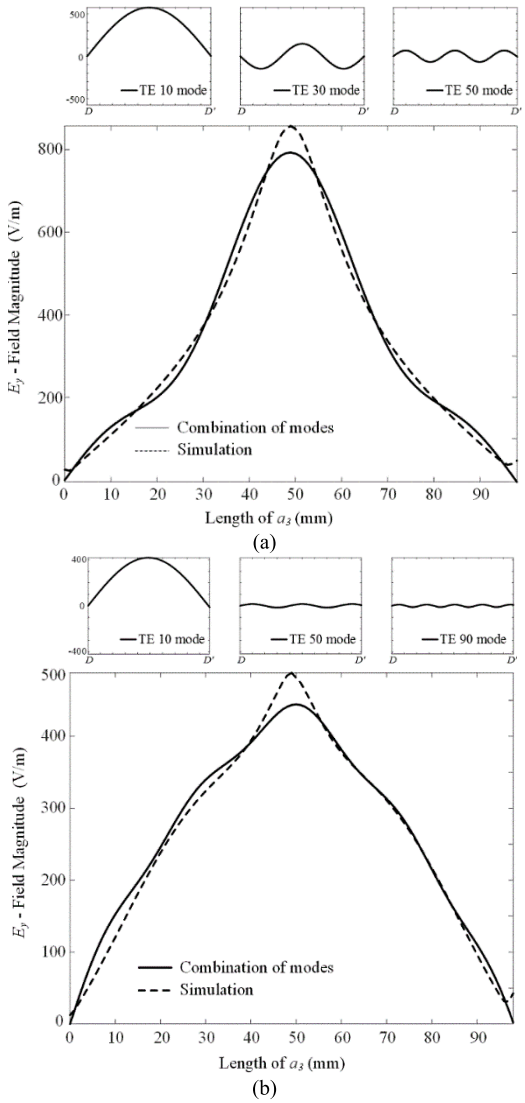

Fig. 9. E_y -field distributions on the $\overline{DD'}$ by comparing between the EM simulation and the combination of modes. (a) 2 GHz. (b) 4 GHz.

functions as follows:

$$\sum_{m=1}^{K_m} A_m \sin(B_m x) \tag{4a}$$

$$\sum_{n=0}^{K_n} C_n \cos(D_n y) \tag{4b}$$

where $B_m = (m\pi/a_3)$ and $D_n = (n\pi/b_3)$.

The coefficients B_m and D_n stand for the eigenvalues along the x- and y-axes. A_m and C_n are the coefficients for each mode, to be solved. Because the E_y-field magnitudes at 2 and 4 GHz vary slightly along the lines $\overline{AA'}$, $\overline{BB'}$, and $\overline{CC'}$, the modes of the fields are assumed to be TE_{m0}, where the second subscript 0 means no variation along the vertical lines. It is therefore important to observe the segment $\overline{DD'}$ to determine the first subscript m that indicates the sinusoids along the x-axis. The resulting cosine function coefficients show that C_0 is dominant compared to the $C_1, C_2, \ldots$, and afterward merged into the coefficients in (4a). On the other hand, the sine function coefficients $A_1, A_3, A_5, \ldots$, have meaningful values, while $A_2, A_4, \ldots$, are almost negligible due to the symmetry. In Fig. 9, the fields in the aperture are decomposed into TE_{m0} modes at 2 and 4 GHz. The E_y-fields obtained by the combination of the decomposed modes are plotted with solid lines, whereas the field calculated using the EM simulation is indicated by the dashed lines. As can be seen, the field at 2 GHz can be decomposed into TE_{10}, TE_{30}, and TE_{50} modes, where the magnitude of TE_{10} mode A_1 is greater than the others, and they decrease gradually as the mode number increases. On the other hand, the field at 4 GHz has the dominant mode TE_{10} that is large enough to ignore the other higher order modes. It is also important that some negative values of the coefficients are essential for making the fluctuating shape in the field pattern. The mode values of the coefficients up to A_9 are listed in Table III. The results demonstrate that the proposed antenna including the horn improves the directivity particularly in the high-frequency band by enhancing the dominant TE_{10} mode.

TABLE III
COEFFICIENTS OF THE MODE DECOMPOSITION

Frequency	A_1	A_3	A_5	A_7	A_9
2 GHz	577.3	-146.8	67.8	-29.0	17.5
4 GHz	416.5	-19.3	14.5	-13.6	8.9

IV. CONCLUSION

The Vivaldi-fed hybrid horn antenna was proposed, which showed a better matching by the AVA in the low-frequency band and an increased gain by the horn in the high-frequency band. Novel aspect of the proposed antenna is that the optimal antenna performances are achieved by hybridizing the advantages of the AVA and the horn antenna. An in-depth study of the hybrids of the AVA and horn was carried out, which has not been conducted in the previous studies. The AVA of the antenna was fabricated by printing the balun, the parallel transmission line and the radiating flares on FR4 substrates. The horn was then made by copper plates surrounding the exterior of the AVA, and the two ends of the flares of the AVA were electrically connected to the external horn. The measured reflection coefficients of the antenna were -11 and -9.1 dB at 1 and 5 GHz, respectively. The improved boresight gains of 5.24 dBi at 1 GHz and 5.35 dBi at 5 GHz were observed, and these gains were higher than both the conventional AVA and the horn antenna of a similar size. The characteristics of the input impedance examined by an equivalent circuit model demonstrated that the operating principle of the proposed antenna in the low-frequency band is similar to that of a conventional Vivaldi antenna. The mode decomposition results showed that the directivity of the antenna is improved by the horn particularly in the high-frequency band due to the enhanced dominant TE_{10} mode. These results confirm that the better characteristics in low frequency matching and high-frequency gain can be achieved by the proposed design. Potentially, the developed antenna can be applied to various applications, such as direction finding, measurement, and acquisition of radio waves, which require wideband operation.

REFERENCES

[1] P. J. Gibson, "The Vivaldi aerial," in *Proc. IEEE 9th Eur. Microw. Conf.*, Sep. 1979, pp. 101–105.
[2] E. Gazit, "Improved design of the Vivaldi antenna," *IEE Proc. H Microw., Antennas Propag.*, vol. 135, no. 2, pp. 89–92, Apr. 1988.
[3] J. Bourqui, M. Okoniewski, and E. C. Fear, "Balanced antipodal Vivaldi antenna with dielectric director for near-field microwave imaging," *IEEE Trans. Antennas Propag.*, vol. 58, no. 7, pp. 2318–2326, Jul. 2010.

[4] J.-B. Yan, S. Gogineni, B. Camps-Raga, and J. Brozena, "A dual-polarized 2–18-GHz Vivaldi array for airborne radar measurements of snow," *IEEE Trans. Antennas Propag.*, vol. 64, no. 2, pp. 781–785, Feb. 2016.

[5] S. H. He, W. Shan, C. Fan, Z. C. Mo, F. H. Yang, and J. H. Chen, "An improved Vivaldi antenna for vehicular wireless communication systems," *IEEE Antenna Wireless Propag. Lett.*, vol. 13, pp. 1505–1508, Jul. 2014.

[6] P. Bolli *et al.*, "From MAD to SAD: The Italian experience for the low-frequency aperture array of SKA1-LOW," *Radio Sci.*, vol. 51, no. 3, pp. 160–175, Mar. 2016.

[7] A. M. D. Oliveira, M. B. Perotoni, S. T. Kofuji, and J. F. Justo, "A palm tree antipodal Vivaldi antenna with exponential slot edge for improved radiation pattern," *IEEE Antennas Wireless Propag. Lett.*, vol. 14, pp. 1334–1337, 2015.

[8] A. Molaei, M. Kaboli, S. A. Mirtaheri, and M. S. Abrishamian, "Dielectric lens balanced antipodal Vivaldi antenna with low cross-polarisation for ultra-wideband applications," *IET Microw., Antennas Propag.*, vol. 8, no. 14, pp. 1137–1142, 2014.

[9] I. T. Nassar and T. M. Weller, "A novel method for improving antipodal Vivaldi antenna performance," *IEEE Trans. Antennas Propag.*, vol. 63, no. 7, pp. 3321–3324, Jul. 2015.

[10] A. Maunder and P. Mousavi, "Application of UWB arrays for material identification of multilayer media in metallic tanks," *IEEE Trans. Antennas Propag.*, vol. 63, no. 11, pp. 4901–4909, Nov. 2015.

[11] S. Chamaani, S. A. Mirtaheri, and M. S. Abrishamian, "Improvement of time and frequency domain performance of antipodal Vivaldi antenna using multi-objective particle swarm optimization," *IEEE Trans. Antennas Propag.*, vol. 59, no. 5, pp. 1738–1742, May 2011.

[12] J.-S. Kang, J.-H. Kim, and J.-I. Park, "Comparison of antenna parameters of R-/S-band standard gain horn antennas," *J. Electromagn. Eng. Sci.*, vol. 15, no. 4, pp. 224–231, Oct. 2015.

[13] M. Manteghi and Y. Rahmat-Samii, "A novel UWB feeding mechanism for the TEM horn antenna, reflector IRA, and the Vivaldi antenna," *IEEE Antennas Propag. Mag.*, vol. 46, no. 5, pp. 81–87, Oct. 2004.

[14] Y. Zhao, Z. Shen, and W. Wu, "Wideband and low-profile H-plane ridged SIW horn antenna mounted on a large conducting plane," *IEEE Trans. Antennas Propag.*, vol. 62, no. 11, pp. 5895–5900, Nov. 2014.

[15] J. Shao, G. Fang, J. Fan, Y. Ji, and H. Yin, "TEM horn antenna loaded with absorbing material for GPR applications," *IEEE Antennas Wireless Propag. Lett.*, vol. 13, pp. 523–527, 2014.

[16] P. Duangtang, P. Mesawad, and R. Wongsan, "Creating a gain enhancement technique for a conical horn antenna by adding a wire medium structure at the aperture," *J. Electromagn. Eng. Sci.*, vol. 16, no. 2, pp. 134–142, Apr. 2016.

[17] S. I. Latif, D. Flores-Tapia, S. Pistorius, and L. Shafai, "Design and performance analysis of the miniaturised water-filled double-ridged horn antenna for active microwave imaging applications," *IET Microw., Antennas Propag.*, vol. 9, no. 11, pp. 1173–1178, Aug. 2015.

[18] D. Oloumi, P. Mousavi, M. I. Pettersson, and D. G. Elliott, "A modified TEM horn antenna customized for oil well monitoring applications," *IEEE Trans. Antennas Propag.*, vol. 61, no. 12, pp. 5902–5909, Dec. 2013.

[19] C. Bruns, P. Leuchtmann, and R. Vahldieck, "Analysis and Simulation of a 1-18-GHz broadband double-ridged horn antenna," *IEEE Trans. Electromagn. Compat.*, vol. 45, no. 1, pp. 55–60, Feb. 2003.

[20] FEKO. (2015). *Altair*. [Online]. Available: http://www.altair.com

[21] J. Yousaf, H. Jung, K. Kim, and W. Nah, "Design, analysis, and equivalent circuit modeling of dual band PIFA using a stub for performance enhancement," *J. Electromagn. Eng. Sci.*, vol. 16, no. 3, pp. 169–181, Jul. 2016.

[22] D. M. Pozar, *Microwave Engineering*, 4th ed. New York, NY, USA: Wiley, 2012.

[23] C. A. Balanis, *Antenna Theory Analysis and Design*, 3rd ed. New York, NY, USA: Wiley, 2005.

[24] M. Amiri, F. Tofigh, A. Ghafoorzadeh-Yazdi, and M. Abolhasan, "Exponential antipodal Vivaldi antenna with exponential dielectric lens," *IEEE Antennas Wireless Propag. Letts.*, vol. 16, pp. 1792–1795, Mar. 2017.

[25] B. Jacobs, J. W. Odendaal, and J. Joubert, "An improved design for a 1–18 GHz double-ridged guide horn antenna," *IEEE Trans. Antennas Propag.*, vol. 60, no. 9, pp. 4110–4118, Sep. 2012.